MDPI

Heterogeneous Activation of Persulfate by LaMO$_3$ (M=Co, Fe, Cu, Mn, Ni) Perovskite Catalysts for the Degradation of Organic Compounds

Donatos Manos [1], Foteini Papadopoulou [1], Antigoni Margellou [1], Dimitrios Petrakis [1,*] and Ioannis Konstantinou [1,2,*]

1 Department of Chemistry, University of Ioannina, 45100 Ioannina, Greece; donatos.manos@yahoo.gr (D.M.); ch04548@uoi.gr (F.P.); amargel@chem.auth.gr (A.M.)

2 Institute of Environment and Sustainable Development, University Research Center of Ioannina (URCI), 45110 Ioannina, Greece

* Correspondence: dpetrakis@uoi.gr (D.P.); iokonst@uoi.gr (I.K.)

Abstract: Sulfate radical-based advanced oxidation processes (SR-AOPs) are lately applied for the degradation of various pollutants through the formation of reactive oxidant species (ROS) from activation of oxidants, such as persulfate (PS) or peroxymonosulfate (PMS). In this study, LaMO$_3$ (M=Co, Fe, Cu, Mn, Ni) perovskite catalysts were synthesized, characterized by several techniques, and tested for the activation of persulfate towards the degradation of phenolic pollutants. The effect of substitution of position B of La-based perovskites as well as calcination temperature was studied. Overall, the results showed that the decisive role in the catalytic activity was the presence of structures that enhance the transfer of electrons between perovskite and oxidant. LaNiO$_3$ followed by LaCoO$_3$ were found as the most active catalysts. Finally, the stability of the catalysts was studied, showing that B-metal leaching is significant for both catalysts, with LaCoO$_3$ being the most stable one.

1. Introduction

Since water resources' pollution is one of the major environmental problems in recent years, environmental and chemical technology is moving towards the development of novel and effective decontamination technologies [1]. This need lies in the fact that most emerging organic pollutants, such as pharmaceuticals, antibiotics, pesticides, etc., are resistant, toxic, and exhibit low biodegradability. As a result, it is practically difficult degrade them with conventional methods [2–4]. As effective methods of decontamination of water and wastewater, advanced oxidation processes (AOPs) are widely applied for the degradation of various resistant pollutants through the formation of reactive oxidant species (ROS), such as hydroxyl ($^\bullet$OH) or sulfate radicals (SO$_4^{\bullet-}$) [5].

A wide variety of AOPs, such as electrochemical [6], photochemical [7], sonochemical [8], photocatalytic, and catalytic processes [9], can be used for the formation of ROS. These processes may differ both in the way in which ROS are formed as well as in the ROS formed. Nevertheless, they can achieve complete or partial degradation of the pollutants in degradation products of much lower toxicity compared to the original ones [10]. Lately, sulfate radical-based advanced oxidation processes (SR-AOPs) are applied for the degradation of various resistant pollutants through the activation of oxidants, such as persulfate (PS) or peroxymonosulfate (PMS), for the formation of ROS [11]. The formation of sulfate radicals is of particular interest to the scientific community, mainly because of the advantages they exhibit over hydroxyl radicals. Some of the main disadvantages of the decontamination methods based on $^\bullet$OH radicals are the limited pH range (2–4) and the creation of sludge in the case of photo-Fenton process [12] and generally the shorter half-life of $^\bullet$OH radicals [13].

The characteristics of sulfate radicals that make them more attractive in decontamination methods are mainly the higher redox potential (2.5–3.1 V for $SO_4^{\bullet-}$ vs. 2.8 V for $^{\bullet}OH$), broader pH range (2–8) of activity [14,15], longer half-life (30–40 $\mu\varsigma$) [16], and the selectivity towards characteristic groups bearing the pollutant toxicity [17].

The main processes that lead to the generation of sulfate radicals or other ROS are through PS and PMS activation. On the one hand, PMS appears as a triple-potassium salt with the formula $2KHSO_5 \cdot KHSO_4 \cdot K_2SO_4$, the so-called Oxone, which is a crystalline solid [18]. Of the three sulfur-containing salts in this formula, the two of them appear as not active for the activation of PMS towards the formation of sulfate radicals [19]. However, PMS is non-toxic, highly soluble in water, and, compared to other oxidants, particularly inexpensive [19]. On the other hand, PS, unlike PMS, displays a symmetrical structure, and the most common forms that can be encountered are potassium-PS ($K_2S_2O_8$), sodium-PS ($Na_2S_2O_8$), or ammonium-PS ((NH_4)$_2S_2O_8$), all colorless or white crystalline solids. In the case of decontamination technologies, potassium or sodium salts are mostly used because of their high solubility, while the use of ammonium salt is avoided due to the secondary contamination resulting from the formation of ammonia [20]. Activation of these oxidizing agents can be carried out using several methods, with each method showing a different mechanism with its advantages and disadvantages, e.g., by electrochemical activation [21], UV-irradiation [22], heat [23,24], transition metal catalysts [25], and metal-free catalysts, such as carbon catalysts [26]. Among these methods, the one that appears most effective is heterogeneous catalysis, mainly due to the low energy requirements, the facile separation after the treatment, and the reusability for several catalytic cycles [27,28]. In contrast, in the case of homogeneous catalysis, a major problem that occurs is the difficult separation of the catalyst, resulting frequently in secondary contamination [29].

Catalysts that have been studied in recent years for PS activation are mainly transition metals and transition metal oxides [30,31]. Particular interest in recent years in the activation of PS seems to be shown by perovskite metal oxides. This is a class of materials with the general formula ABO_3, where A and B can be occupied by metal cations and, specifically, A being the larger-sized rare earth or alkaline earth metal, B a 3d transition metal, and O is oxygen [32]. Based on the general structure of perovskite, oxygen is the connecting link between the A cation, which is situated at the corners of this cubic structure, and the smaller B cation, which is situated at the center [33]. However, the cubic structure is not the only one that occurs in perovskites, and depending on the cations that occupy the A and B positions, other structures, such as rhombohedral, hexagonal, tetragonal, and orthorhombic ones, can be formed [34]. Perovskites, in addition to the simple ABO_3 form mentioned before, can exist in other forms as well, such as A_2BO_4 (layered perovskite), $A_2BB'O_6$ (double perovskite), or $A_2A'B_2B'O_9$ (triple perovskite), which show even more complex structures [34]. These are materials that have the potential to incorporate many different metal cations into their structure and substitute the cations of positions A and B without destroying their original structure. Still, due to this structure, they are able to incorporate more than 90% of the metallic elements found in the periodic table, while by differentiating the synthesis method, it is possible to obtain materials with different physicochemical properties [35]. Consequently, all these features make perovskites attractive in a multitude of applications, such as sensors and biosensors [36], solar cells and solid oxide fuel cells [37], adsorbents [38], catalysis [39], etc.

Many studies have been presented on the use of perovskites in decontamination technologies through oxidation processes, with emphasis being placed not only on the presence of the various metal ions at the A and B sites of the perovskite structure but also on how these materials are synthesized. For example, the prevalence of Co^{2+} as the metal ion of position B has been reported in the degradation of organic pollutants through oxidation processes, while studies have also been presented on Fe^{2+} [39,40], Mn^{2+} [41,42], Ni^{2+} [43], Cu^{2+} [44], and others. However, regarding the position A of the perovskite structure, it seems that lanthanum has prevailed, as the plethora of research studies that have appeared in recent years mainly concern lanthanum-based perovskites.

In this paper, we focus on the synthesis by the surfactant combustion method of a series of lanthanum-based perovskites with different metal ions in position B of the perovskite structure (LaMO$_3$, M=Co, Fe, Cu, Mn, Ni). The synthesized perovskites were characterized by several techniques, and their catalytic activity in terms of the degradation of phenolic compounds by activation of PS was subsequently studied. In the catalytic activity experiments, phenol was used as a standard pollutant, as it belongs to a class of compounds that not only shows high levels of toxicity and has harmful effects on the human body but also on that of animals [45]. In addition, for the most active material, the effect of the calcination temperature during the synthetic method on the catalytic activity was also studied.

2. Results and Discussion

2.1. Characterization of LaMO$_3$

The x-ray diffraction patterns of synthesized perovskite materials are presented in Figure 1. First, diffractograms of LaMnO$_3$ and LaFeO$_3$ materials show the formation of well crystalline perovskite structures with LaFeO$_3$ presenting orthorhombic phase while LaMnO$_3$ presents triangular and cubic perovskite phase. These findings are in agreement with analogous materials synthesized by Rao et al. 2018 [46] and Zhang et al. 2018 [47] for LaFeO$_3$ and Wang et al. 2019b [48] for LaMnO$_3$ although different synthesis approaches have been used, i.e., sol-gel citric acid method for LaFeO$_3$ and hydrothermal-PVP method for LaMnO$_3$.
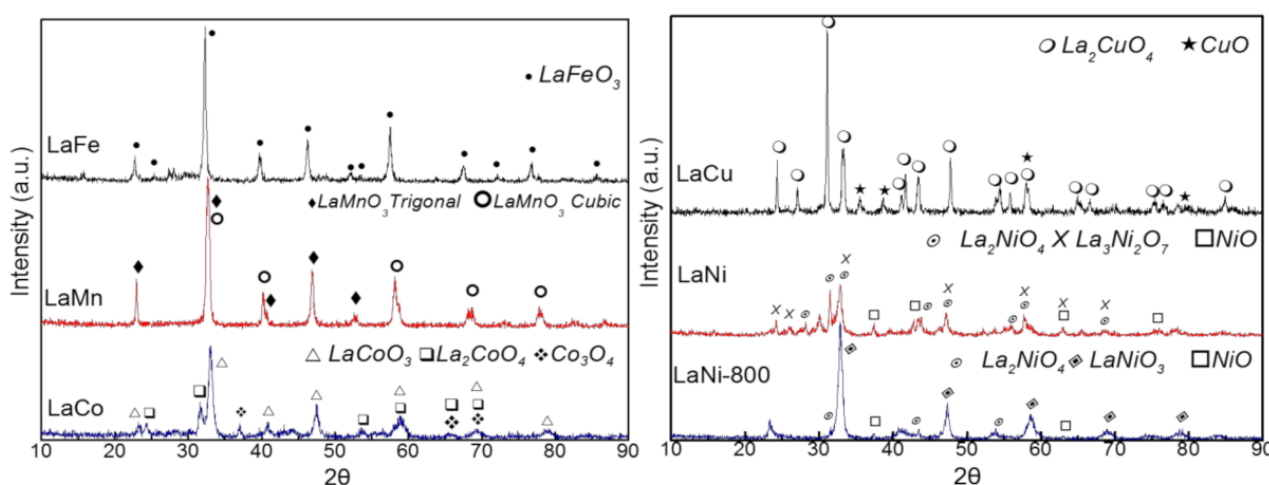

Figure 1. XRD patterns of LaMO$_3$ perovskites.

For LaCoO$_3$, LaNiO$_3$, and LaCuO$_3$, the diffractograms showed a diversity in the crystalline phases formed. LaCoO$_3$ presented three phases, with perovskite mono-clinic structure being the more abundant one, followed by orthorhombic perovskite Ruddlesden–Popper (RP) structure and cobalt oxide with cubic structure. In the cases of Hammouda et al. 2017 [49] and Guo et al. 2020 [50], where citric acid sol-gel method was used, cubic and rhombohedral structures occurred, respectively. LaNiO$_3$ also presents three phases, with a greater percentage of orthorhombic RP and smaller percentages of homologous perovskite structure with orthorhombic structure and oxide with triangular structure. In the case of synthesized perovskite with citric acid sol-gel method [40], a cubic structure is reported. LaCuO$_3$ consists of two phases, the main one being orthorhombic RP and, in a smaller percentage, monoclinic oxide, while in the case of Lin et al. (2017) [43], where glycine-combustion preparation method was followed, peaks corresponding to oxides are presented to a small extent, and the main structure corresponds to the rhombohedral structure. Based on the XRD diagram, LaCuO$_3$ perovskite exhibits a higher crystallinity degree as compared to the other catalysts. Finally, for the LaNiO$_3$ material that was also calcined at 800 °C (LaNiO$_3$-800), it was found that the Ruddlesden–Popper perovskite

structure decreased, and the largest percentage is found in the classical ABO_3 structure. Table 1 shows details of the crystalline phases, as identified by the Match program. The RP designation next to the phases corresponds to RP-perovskite from the Ruddlesden–Popper homologous perovskite series.

Table 1. Textural properties of the synthesized perovskites $LaMO_3$.

Perovskite	Crystalline Phase (% Content)	Specific Surface Area (m^2/g)
$LaMnO_3$	$LaMnO_3$-P-trigonal (74%) $LaMnO_3$-P-Cubic (26%)	13
$LaFeO_3$	$LaFeO_3$-P-orthorombic (100%)	14
$LaCoO_3$	$LaCoO_3$-P-monoclinic (70%) La_2CoO_4-RP-orthorhombic (18%) Co_3O_4-O-cubic (12%)	7
$LaNiO_3$	La_2NiO_4-RP-orthorhombic (50%) $La_3Ni_2O_7$-HS-orthorhombic (28%) NiO-O-trigonal (22%)	13
$LaCuO_3$	La_2CuO_4-RP-orthorombic (80%) CuO-O-monoclinic (20%)	7
$LaNiO_3$-800	$LaNiO_3$-P-trigonal (69%) La_2NiO_4-RP-tetragonal (25%) NiO-O-trigonal (6%)	5

Nitrogen adsorption-desorption isotherms at 77 K for all studied materials are shown in Figure 2. For $LaMnO_3$, $LaFeO_3$, $LaCoO_3$, and $LaNiO_3$, the isotherms obtained are of type IV with a hysteresis loop of type H2(b) according to IUPAC classification [51] corresponding to mesoporous materials. The specific surface area ranged from 7 m^2/g for $LaCoO_3$ to 14 m^2/g for $LaFeO_3$, which is a similar range to several perovskites in the literature [50,52] although there are also cases where synthesized perovskites display specific surface areas in the order of 60–120 m^2/g [53,54], while the respective pore diameters were 18.4 Å and 88.9 Å. On the other hand, $LaCuO_3$ and $LaNiO_3$-800 materials appear as non-porous and adsorption-desorption isotherms are of type II with H2(b) type hysteresis loop. Their specific surface areas display values of 7 m^2/g and 5 m^2/g, respectively. Hydrodynamic particle sizes have been also measured by dynamic light scattering (DLS). Median particle diameters were 0.221, 0.250, 0.288, 0.392, and 2.018 μm for $LaNiO_3$, $LaMnO_3$, $LaFeO_3$, $LaCoO_3$, and $LaCuO_3$, respectively.

Scanning electron microscopy (SEM) was used to reveal the morphology of synthesized perovskites. Based on the microphotographs from all samples for various magnifications (Figure 3), it was observed that none of the materials show a clear geometric crystalline shape. $LaMnO_3$ appears to have a uniform spongy texture, and $LaFeO_3$ appears to have a partly spongy texture, while its surface appears to be rougher than $LaMnO_3$. Moreover, $LaCoO_3$, is also partly spongy, but the interstices between them appear to be more spaced than in the previous cases. The above texture characteristics are consistent with results reported elsewhere [40]. $LaNiO_3$ appears to exhibit a spongy texture as well, which was retained after calcination to 800 °C. $LaCuO_3$ seems to be more "fragmented," while at the same time, there are larger aggregates in size, and the expected interstices that would make it spongy are not observed.

2.2. Activation of Persulfate by $LaMO_3$ towards Phenolics Degradation

2.2.1. Effect of B-position Metal Ion and Calcination Temperature

According to Figure 4, depending on the metal cation that occupies the B position of each perovskite catalyst, a significant differentiation was observed in the degradation rate of phenolics. The catalytic activity followed the trend: $LaNiO_3$ > $LaCoO_3$ > $LaCuO_3$ > $LaMnO_3$ > $LaFeO_3$, with the corresponding rate constants of 0.082 min^{-1}, 0.029 min^{-1}, 0.006 min^{-1}, 0.0009 min^{-1}, and 0.00004 min^{-1} (Table 2). Apparently, there is no correlation between the specific surface area of perovskites and their catalytic activity. On the

other hand, the presence of two different oxidation states of the metal in position B in the structure of perovskites appears to play a decisive role in their catalytic activity, making easier electron transfer processes between the surface of the perovskites and the oxidant, as it has been reported also elsewhere [42]. For example, in the case of $LaCuO_3$ (La_2CuO_4-RP-orthorombic 80%), it has been reported that copper is present as Cu(I) and Cu(II) [55]. In addition, RP-perovskite structures showed excellent variability in lattice oxygen and charge-transfer ability. The co-presence of RP and single-perovskite structure was demonstrated to exhibit superior activity for phenol degradation as compared to pure-phase perovskite materials. The higher activity was attributed to the higher amount of generated oxygen vacancies, the stronger affinity of perovskite surface to the reactants (PMS and phenol), and the higher electron conduction efficiency [56]. In consistency, the catalysts presenting mixed RP and single-perovskite structures were the more efficient ones in the present study.
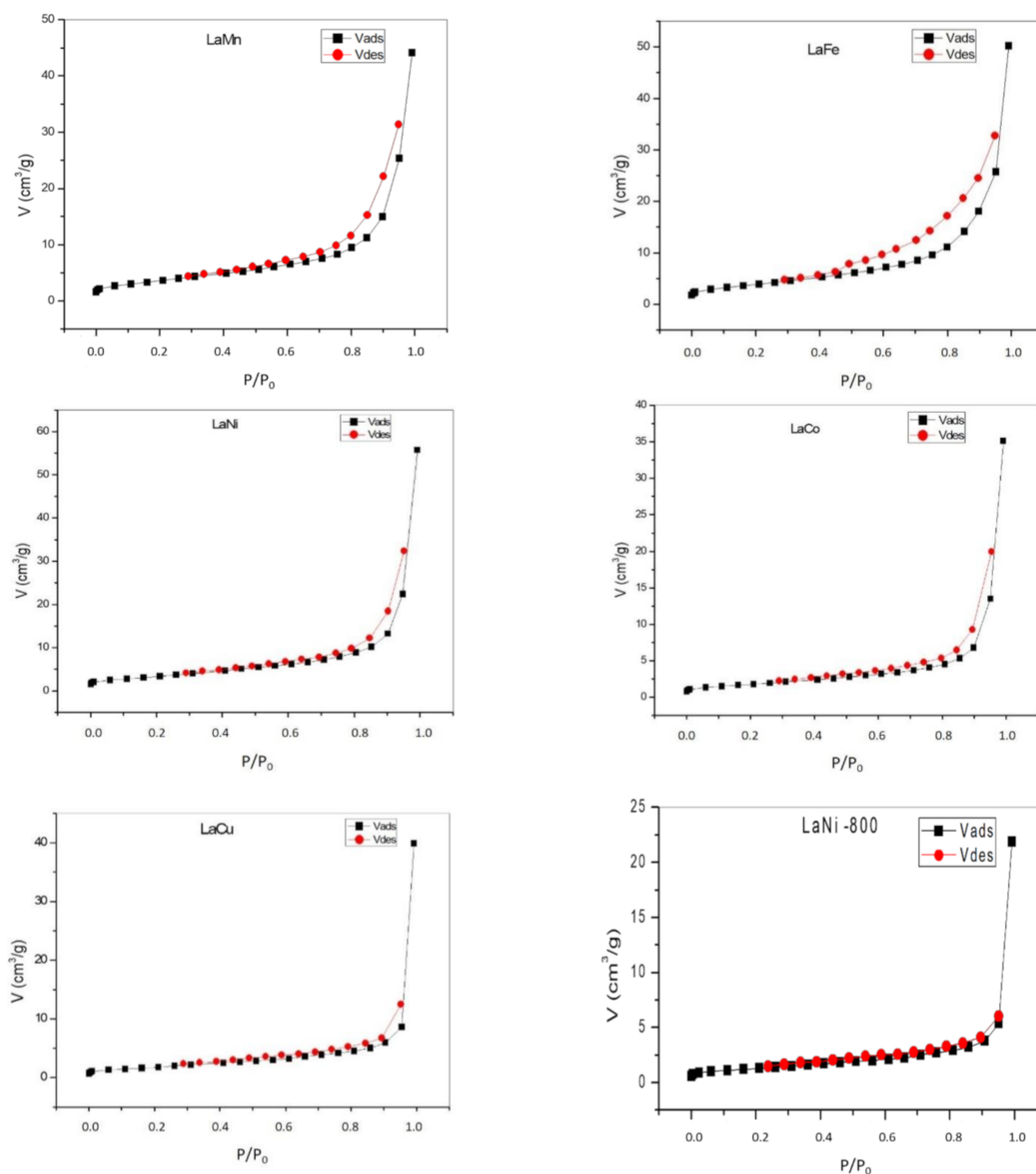

Figure 2. N_2 adsorption-desorption isotherms of $LaMO_3$ (M=Co, Fe, Cu, Mn, Ni) perovskites.

Figure 3. SEM microphotographs of (**a**) LaMnO$_3$; (**b**) LaFeO$_3$; (**c**) LaCoO$_3$; (**d**) LaNiO$_3$; (**e**) LaCuO$_3$; and (**f**) LaNiO$_3$-800.
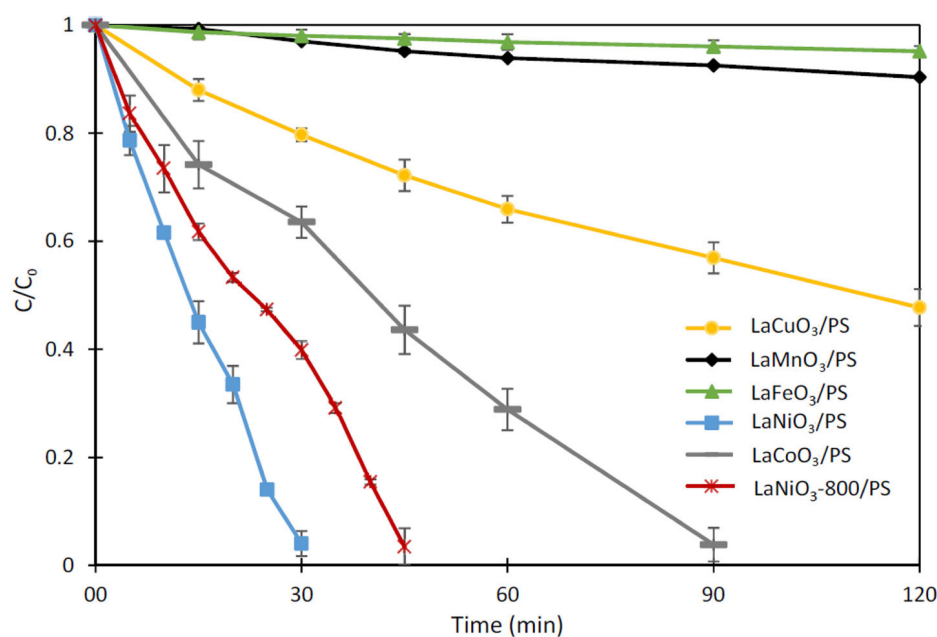
Figure 4. Degradation of phenolics in different reaction systems (catalyst = 0.25 g L^{-1}, PS = 10 mM, phenol = 10 mgL^{-1}).

Table 2. Catalytic activity of the LaMO$_3$ (M=Co, Fe, Cu, Mn, Ni) perovskites.

Perovskite	(%) Degradation	k (min^{-1})	R^2
LaMnO$_3$	10% in 120 min	0.0009	0.9696
LaFeO$_3$	5% in 120 min	0.00004	0.9625
LaCoO$_3$	96% in 90 min	0.029	0.9258
LaNiO$_3$	96% in 30 min	0.082	0.9344
LaCuO$_3$	52% in 120 min	0.006	0.9925
LaNiO$_3$-800	97% in 45 min	0.048	0.9248

Since LaNiO$_3$ was the most active material in terms of phenolic degradation, the effect of calcination temperature was studied at a higher calcination temperature 800 °C (vs. 600 °C). As can be seen in Figure 4, the catalytic activity of LaNiO$_3$-800 is reduced compared to that calcined at 600 °C. The increase in calcination temperature led to a material that retained its original spongy structure but with a lower specific surface area, the lowest of all previous materials, and a significant variation of the % phase content, with single-LaNiO$_3$ phase prevailing. As a result, the ratio of RP to single-perovskite structure plays a significant role in the catalytic efficiency. However, LaNiO$_3$-800 is still more active than all the other materials with a different B-cation, which reinforces the consideration that crystal phase ratio and the co-current presence of phases with different oxidation states of B-metal is the crucial parameter affecting the activity.

Table 3 summarizes previous data for phenol degradation through persulfate activation with perovskite catalysts. For comparison to the most active materials presented in this research, it should be taken into consideration the different method of substrate determination. The previous studies [56–59] monitored the degradation of initial phenol concentration by HPLC, while the current method monitored the removal of the total phenolic content (phenol plus phenolic transformation products formed during the process). LaCoO$_3$ displays comparable efficiency (k = 0.029 min^{-1}) to the lower values reported among the other materials. On the other hand, LaNiO$_3$ displays the second best rate constant (0.082 min^{-1}) (Table 3).

Table 3. Performance of various perovskite systems for phenol degradation.

Catalyst	(%) Degradation	k (min^{-1})	Metal Leaching (mgL^{-1})	Reference
$LaCo_{0.5}Mn_{0.5}O_{3+\delta}$	100% in 60 min	0.052	Co: 4.07	[57]
$La_{0.4}Sr_{0.6}MnO_{3-\delta}$	100% in 90 min	0.031	Mn: 1.11 Sr: 8.91	[58]
$LaCo_{0.6}Cu_{0.4}O_3$	99% in 12 min	0.302	Co: 1.37	[59]
$La_{0.4}Sr_{1.05}MnO_{4-\delta}$	100% in 60 min	0.070	Mn: 3.20 Sr: 4.04	[56]
$LaCoO_3$	96% in 90 min	0.029	Co: 1.34	This work
$LaNiO_3$	96% in 30 min	0.082	Ni: 14.39	This work

2.2.2. Quenching Experiments for the Determination of ROS

Three different scavengers were used in order to elucidate the degradation mechanism and the dominant ROS generated during the treatment. Tert-butanol (TBA), which does not contain α-hydrogens, was used as a scavenger for the generated $^\bullet OH$, as it reacts rapidly with the produced hydroxyl radicals. Ethanol (EtOH), which contains α-hydrogens, was used as scavenger for both hydroxyl and sulfate radicals [60], and NaN_3 was used as a scavenger for both $^\bullet OH$ and $SO_4^{\bullet-}$ radicals as well as singlet oxygen ($^1O_2$) [61]. Since the predominance of the synthetic method with the calcination temperature at 600 °C versus 800 °C was presented, the materials that will be studied in terms of the degradation mechanism of phenolics are the most active of this series, namely $LaCoO_3$ and $LaNiO_3$.

As mentioned above, in the case of the $LaCoO_3$/PS system, phenol degradation of 96% was observed in just 90 min, with a corresponding rate constant of 0.029 min^{-1}. In the presence of both TBA and EtOH, a minimal decrease in phenol degradation was observed, as shown by the Figure 5a, to 89% and 87% over 90 min, respectively, which means that the formation of $^\bullet OH$ contributes in a greater percentage to the degradation of phenolics and, in a smaller percentage, of $SO_4^{\bullet-}$. However, in the case when NaN_3 was used as a scavenger, a decrease in phenolic degradation was observed to a greater extent. Particularly, a decrease in phenol degradation was observed from 96% in the absence of a scavenger to 82% in 90 min, with the corresponding rate constant decreasing from 0.029 min^{-1} to 0.015 min^{-1}. Thus, in the $LaCoO_3$/PS system, $^1O_2$ and $^\bullet OH$ had a greater contribution to the degradation of phenolics while $SO_4^{\bullet-}$ were formed in a minor amount.

Additionally, in the case of the $LaNiO_3$/PS system, as can be seen from the Figure 5b, the inhibition in the presence of azide ions predominates since there is a decrease in the degradation of phenolics from 96% (k = 0.082 min^{-1}) in the absence of a scavenger to 71% (0.030 min^{-1}) within 30 min. A significant decrease is also observed in the cases where TBA and EtOH were used as scavengers. Specifically, in the case of EtOH, there was a decrease in phenol degradation to 76% in 30 min, with the corresponding rate constant of 0.042 min^{-1}, while in the case of TBA, there was a decrease to 86% in 30 min with the rate constant of 0.053 min^{-1}. This means that all the three ROS, namely $^1O_2$, $^\bullet OH$, and $SO_4^{\bullet-}$, were formed and contributed the degradation of phenolics.

2.2.3. Reusability and Stability of the Best Catalysts

The stability-reusability of $LaCoO_3$ and $LaNiO_3$ catalysts for three catalytic cycles was studied (Figure 6). In the $LaCoO_3$/PS system, it is evident that the catalyst performance is not affected after three catalytic cycles. In the first two cycles, the degradation of phenol remained stable at 96%, while in the third cycle, there was a slight decrease at 89%. However, this is not observed in the case of the $LaNiO_3$/PS system, as there is a gradual decrease in the catalytic activity of perovskite, i.e., from 96% in the first cycle to 90% in the second cycle, followed by a greater decrease in the third cycle, down to 58%.
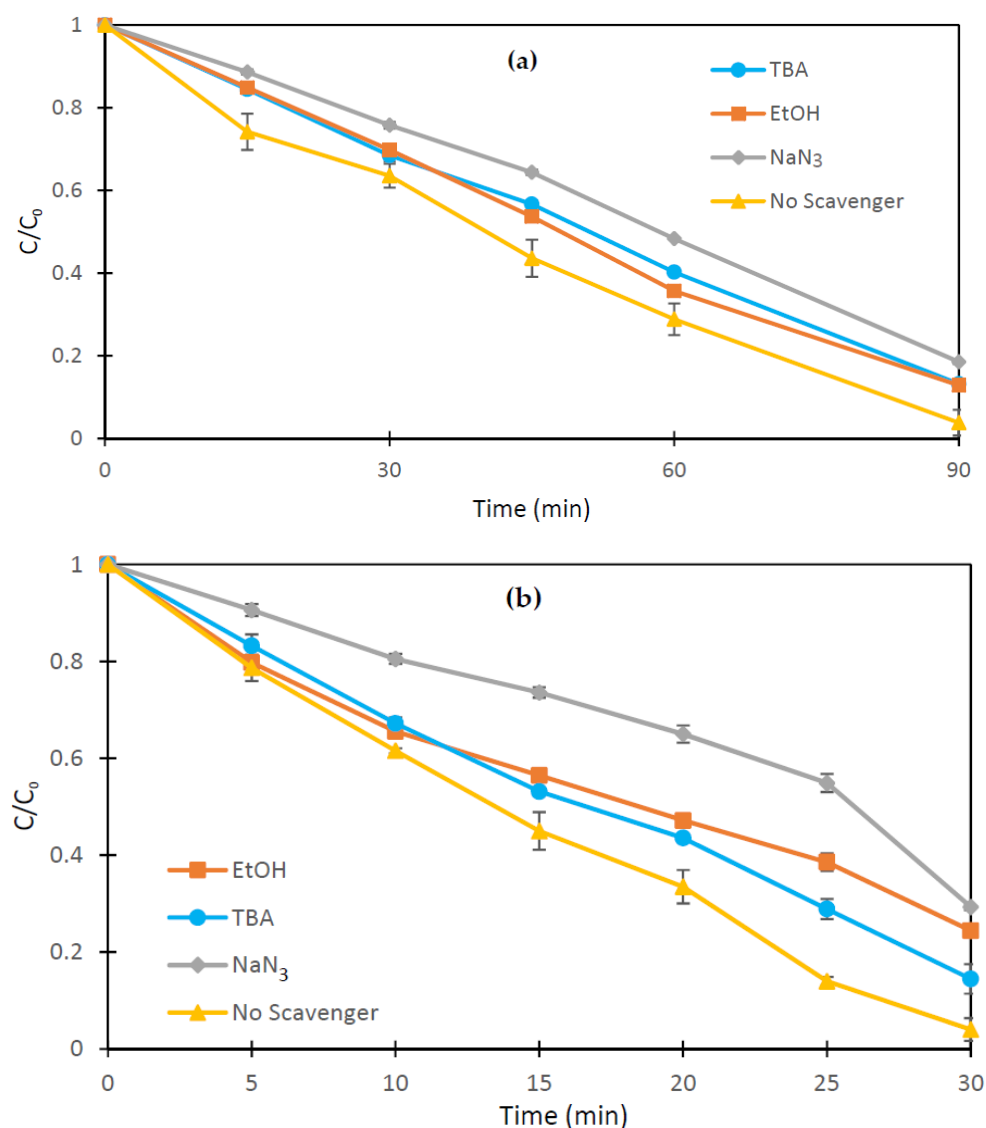
Figure 5. Degradation of phenolics in the presence of scavengers; (**a**) $LaCoO_3/PS$ and (**b**) $LaNiO_3/PS$ system (catalyst = 0.25 g L^{-1}, PS = 10 mM, phenol = 10 mgL^{-1}, scavenger= 0.1 M).

Metal leaching was studied as well in order to correlate with the reusability of the catalysts since gradual metal release leads to their deactivation [62]. As observed in Figure 7, there is a gradual increase with a rather constant rate in the amount of cobalt lost from $LaCoO_3$ perovskite, with the total concentration after the third cycle being approximately 6.6 mgL^{-1}. In the case of $LaNiO_3$, higher concentrations of nickel ion were detected, i.e., 14.39 mgL^{-1} for the first cycle to 17.24 mgL^{-1} for the third cycle. The subsequent gradual increase in the metal losses after each catalytic cycle has been reported to affect the surface properties of perovskites and thus explains the corresponding decrease in their catalytic activity [50]. Metal leaching in these cases can be due to two reasons: either the existence of even a small degree of water solubility of the catalyst (due to the oxides of the metals they may contain) [63] or the formation of water-soluble products that can result from the reaction of the catalyst with the solvent-oxidant system [64]. Thus, comparing these two materials in terms of their stability, the prevalence of $LaCoO_3$ over $LaNiO_3$ is significant.
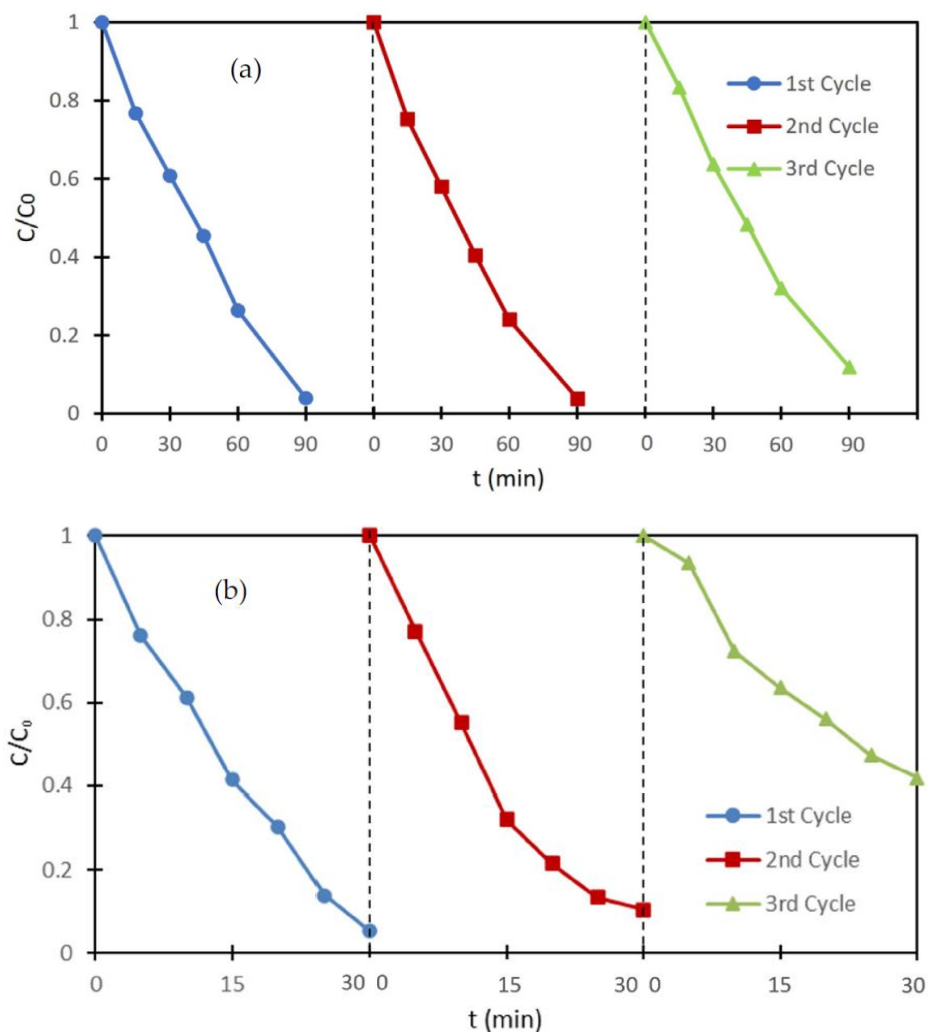
Figure 6. Catalytic performance after three consecutive cycles of (**a**) LaCoO$_3$/PS and (**b**) LaNiO$_3$/PS system (catalyst = 0.25 g L^{-1}, PS = 10 mM, phenol = 10 mgL^{-1}).
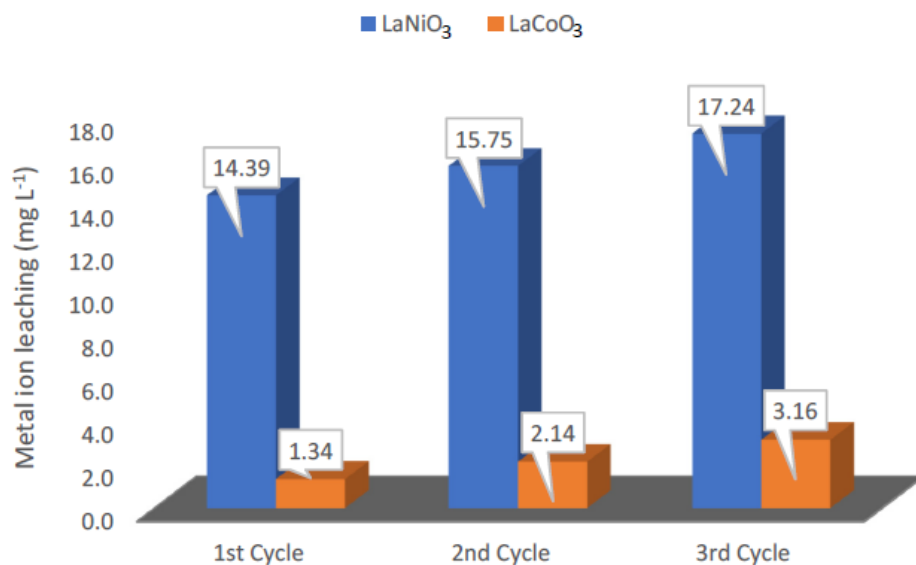

Figure 7. Metal (Co, Ni) leaching in the reaction media during each catalytic cycle from the most active catalysts.

3. Materials and Methods

3.1. Materials

For perovskite synthesis, nitrates La(NO$_3$)$_3$ · 6H$_2$O, Mn(NO$_3$)$_2$ · 4H$_2$O, Cu(NO$_3$)$_2$ · 2.5H$_2$O, Ni(NO$_3$)$_2$ · 5H$_2$O, Co(NO$_3$)$_2$ · 6H$_2$O (≥98.0%, Fluka, Steinheim, Germany), and Fe(NO$_3$)$_3$ · 9H$_2$O (≥99.0%, Merck, Darmstadt, Germany) were used as cation precursors. Glycolic acid ethoxylate lauryl ether (≥99.0%, Aldrich, St. Louis, MO, USA) was used in the synthesis in the presence of the anionic surfactant, while the pH adjustment was carried out with 1N HNO$_3$ (Fixanal, Fluka, Seelze, Germany). For the perovskite catalytic activity control experiments, phenol (99% purity), sodium azide (NaN$_3$), and Folin–Ciocalteu's phenol reagent were obtained from Merck (Germany). Methanol (MeOH, ≥99.8%), ethanol (EtOH), tert-butanol (TBA), sodium carbonate anhydrous (Na$_2$CO$_3$, ≥99.8%), and sodium persulfate (Na$_2$S$_2$O$_8$, ≥98.0%) were purchased from Sigma-Aldrich. All chemicals were used without further purification, and distilled water was used in all experiments.

3.2. Synthetic Method of LaMO$_3$

The synthesis of perovskites was carried out in the presence of the anionic surfactant glycolic acid ethoxylate lauryl ether. Initially, 100 mL of 0.05 M solution of anionic surfactant were stirred for 10 min at 25 °C, 1N HNO$_3$ was added to adjust the pH = 1.00, and then, the solution was stirred for 1h. Then, determined volumes of 0.05 M La(NO$_3$)$_3$ · 6H$_2$O were added, and the mixture was left under stirring for 1h. Afterwards, determined volumes of the corresponding metal nitrate hydrate reagents was added and stirred for 24 h. Finally, the obtain solids were dried at 90 °C and then calcinated at 600 °C for 6 h under atmospheric conditions. Best catalyst (LaNiO$_3$) was also calcined at 800 °C for comparison in the catalytic activity.

3.3. Characterization of LaMO$_3$

X-ray diffraction (XRD) patterns of the synthesized materials were obtained using a D8 Bruker Advance diffractometer with a monochromatic radiation Cu-Ka (λ = 1.5406 Å) in the scanning range 10° ≤ 2θ ≤ 90° and scanning rate of 0.01°/s. The samples were measured in powder form after they were calcined. Identification of crystal phases was carried out via the trial version of Match! 3 Software (Crystal impact, Bonn, Germany).

The surface area of the synthesized materials was measured by adsorption-desorption N$_2$. Adsorption-desorption isotherms were obtained with the Autosorb-1 porosimeter at a liquid nitrogen temperature of 77 K, using a 9-mm measuring cell with the corresponding rod. Degassing of materials at 180 °C for 5 h was required before the measurement. The surface morphology of the particles was observed in a Jeol JSM 5600 system operating at 20 kV. Prior to the analysis, the solids were sputtered with gold under argon atmosphere. A Shimadzu SALD-2300 laser diffraction particle size analyzer (Kyoto, Japan) working with dynamic light scattering (DLS) mode was used for the hydrodynamic particle size measurements.

3.4. Catalytic Activity of LaMO$_3$ Materials

Phenolics degradation experiments were carried out in 200-mL conic flasks containing 100 mL of phenol aquatic solution with an initial concentration of 10 mgL^{-1} and specific amounts of catalyst (LaMO$_3$) under continuous stirring, at room temperature. In order to start the reaction, oxidant (sodium persulfate) was added into the reactor. Then, at predetermined time intervals, 6 mL of the reaction solution were withdrawn, quenched immediately with methanol to terminate the oxidation reaction, and filtered by 0.45-μm membrane filter. Finally, 5 mL of the collected sample were used for the determination of phenolics concentration by Folin–Ciocalteu method [65] using a UV/Vis spectrophotometer (V-360, Jasco, Tokyo, Japan). The reusability of the catalysts with the best activity was studied through catalytic cycle experiments following the previous procedures. At the end of each catalytic cycle, the catalyst was collected and rinsed with distilled water. The stability of the best catalysts was also studied by determining the concentration of

the leached B metals (Co, Ni) at the end of each catalytic cycle, utilizing ICP-MS/Laser Ablation technique. The analysis was performed using a NWR213 laser ablation system (Elemental Scientific, Omaha, NE, USA) attached to an iCAP Q-ICP-MS unit (Thermo Scientific, Waltham, MA, USA).

4. Conclusions

The choice of the metal ion at position B of the perovskite structure appears to significantly affect the properties of the synthesized perovskites, including both their surface properties and the catalytic activiou. Of the series of perovskites synthesized, the most active for persulfate activation and subsequent degradation of phenolics was $LaNiO_3$ followed by $LaCoO_3$. The co-presence of RP and single-perovskite structure was demonstrated to exhibit superior activity. Still, it was shown that the increase in calcination temperature resulted in lower catalytic activity. Finally, the use of $LaCoO_3$ and $LaNiO_3$ for consecutive catalytic cycles revealed better recyclability and lower metal leaching for $LaCoO_3$. Further techniques aiming at diminishing metal losses should be considered in future research.

Author Contributions: Conceptualization, I.K. and D.P.; methodology, D.P.; formal analysis, D.M., F.P. and A.M.; investigation, D.M., F.P. and A.M.; resources, I.K. and D.P.; writing—original draft preparation, D.M. and I.K.; writing—review and editing, D.M., D.P. and I.K.; visualization, D.M. and F.P.; supervision, I.K. and D.P; funding acquisition, I.K. and D.P. All authors have read and agreed to the published version of the manuscript.

References

1. Schwarzenbach, R.P.; Escher, B.I.; Fenner, K.; Hofstetter, T.B.; Johnson, C.A.; von Gunten, U.; Wehrli, B. The Challenge of Micropollutants in Aquatic Systems. *Science* **2006**, *313*, 1072–1077. [CrossRef]
2. Arman, N.Z.; Salmiati, S.; Aris, A.; Salim, M.R.; Nazifa, T.H.; Muhamad, M.S.; Marpongahtun, M. A Review on Emerging Pollutants in the Water Environment: Existences, Health Effects and Treatment Processes. *Water* **2021**, *13*, 3258. [CrossRef]
3. Babuponnusami, A.; Muthukumar, K. A Review on Fenton and Improvements to the Fenton Process for Wastewater Treatment. *J. Environ. Chem. Eng.* **2014**, *2*, 557–572. [CrossRef]
4. Wang, H.; Xi, H.; Xu, L.; Jin, M.; Zhao, W.; Liu, H. Ecotoxicological Effects, Environmental Fate and Risks of Pharmaceutical and Personal Care Products in the Water Environment: A Review. *Sci. Total Environ.* **2021**, *788*, 147819. [CrossRef] [PubMed]
5. Zhang, T.; Zhu, H.; Croué, J.-P. Production of Sulfate Radical from Peroxymonosulfate Induced by a Magnetically Separable $CuFe_2O_4$ Spinel in Water: Efficiency, Stability, and Mechanism. *Environ. Sci. Technol.* **2013**, *47*, 2784–2791. [CrossRef] [PubMed]
6. Sun, Z.; Li, S.; Ding, H.; Zhu, Y.; Wang, X.; Liu, H.; Zhang, Q.; Zhao, C. Electrochemical/Fe^{3+}/Peroxymonosulfate System for the Degradation of Acid Orange 7 Adsorbed on Activated Carbon Fiber Cathode. *Chemosphere* **2020**, *241*, 125125. [CrossRef] [PubMed]
7. Kilic, M.Y.; Abdelraheem, W.H.; He, X.; Kestioglu, K.; Dionysiou, D.D. Photochemical Treatment of Tyrosol, a Model Phenolic Compound Present in Olive Mill Wastewater, by Hydroxyl and Sulfate Radical-Based Advanced Oxidation Processes (AOPs). *J. Hazard. Mater.* **2019**, *367*, 734–742. [CrossRef] [PubMed]
8. Ferkous, H.; Merouani, S.; Hamdaoui, O.; Pétrier, C. Persulfate-Enhanced Sonochemical Degradation of Naphthol Blue Black in Water: Evidence of Sulfate Radical Formation. *Ultrason. Sonochem.* **2017**, *34*, 580–587. [CrossRef]
9. Liu, G.; Zhou, Y.; Teng, J.; Zhang, J.; You, S. Visible-Light-Driven Photocatalytic Activation of Peroxymonosulfate by $Cu_2(OH)PO_4$ for Effective Decontamination. *Chemosphere* **2018**, *201*, 197–205. [CrossRef]
10. Oh, W.-D.; Dong, Z.; Lim, T.-T. Generation of Sulfate Radical through Heterogeneous Catalysis for Organic Contaminants Removal: Current Development, Challenges and Prospects. *Appl. Catal. B Environ.* **2016**, *194*, 169–201. [CrossRef]
11. Duan, X.; Su, C.; Miao, J.; Zhong, Y.; Shao, Z.; Wang, S.; Sun, H. Insights into Perovskite-Catalyzed Peroxymonosulfate Activation: Maneuverable Cobalt Sites for Promoted Evolution of Sulfate Radicals. *Appl. Catal. B Environ.* **2018**, *220*, 626–634. [CrossRef]

12. Yang, Q.; Choi, H.; Al-Abed, S.R.; Dionysiou, D.D. Iron-Cobalt Mixed Oxide Nanocatalysts: Heterogeneous Peroxymonosulfate Activation, Cobalt Leaching, and Ferromagnetic Properties for Environmental Applications. *Appl. Catal. B Environ.* **2009**, *88*, 462–469. [CrossRef]

13. Machulek, A.; Oliveira, C.S.; Osugi, M.E.; Ferreira, V.S.; Quina, F.H.; Dantas, R.F.; Oliveira, S.L.; Casagrande, G.A.; Anaissi, F.J.; Silva, V.O.; et al. Application of Different Advanced Oxidation Processes for the Degradation of Organic Pollutants. In *Organic Pollutants—Monitoring, Risk and Treatment*; IntechOpen, Ltd.: London, UK, 2013. [CrossRef]

14. Zhang, B.-T.; Zhang, Y.; Teng, Y.; Fan, M. Sulfate Radical and Its Application in Decontamination Technologies. *Crit. Rev. Environ. Sci. Technol.* **2015**, *45*, 1756–1800. [CrossRef]

15. Tsitonaki, A.; Petri, B.; Crimi, M.; Mosbæk, H.; Siegrist, R.L.; Bjerg, P.L. In Situ Chemical Oxidation of Contaminated Soil and Groundwater Using Persulfate: A Review. *Crit. Rev. Environ. Sci. Technol.* **2010**, *40*, 55–91. [CrossRef]

16. Mahdi Ahmed, M.; Barbati, S.; Doumenq, P.; Chiron, S. Sulfate Radical Anion Oxidation of Diclofenac and Sulfamethoxazole for Water Decontamination. *Chem. Eng. J.* **2012**, *197*, 440–447. [CrossRef]

17. Hu, P.; Long, M. Cobalt-Catalyzed Sulfate Radical-Based Advanced Oxidation: A Review on Heterogeneous Catalysts and Applications. *Appl. Catal. B Environ.* **2016**, *181*, 103–117. [CrossRef]

18. Wacławek, S.; Grübel, K.; Černík, M. Simple Spectrophotometric Determination of Monopersulfate. *Spectrochim. Acta Part A Mol. Biomol. Spectrosc.* **2015**, *149*, 928–933. [CrossRef]

19. Wacławek, S.; Lutze, H.V.; Grübel, K.; Padil, V.V.T.; Černík, M.; Dionysiou, D.D. Chemistry of Persulfates in Water and Wastewater Treatment: A Review. *Chem. Eng. J.* **2017**, *330*, 44–62. [CrossRef]

20. Behrman, E.J.; Dean, D.H. Sodium Peroxydisulfate Is a Stable and Cheap Substitute for Ammonium Peroxydisulfate (Persulfate) in Polyacrylamide Gel Electrophoresis. *J. Chromatogr. B Biomed. Sci. Appl.* **1999**, *723*, 325–326. [CrossRef]

21. Cai, C.; Zhang, H.; Zhong, X.; Hou, L. Electrochemical Enhanced Heterogeneous Activation of Peroxydisulfate by Fe-Co/SBA-15 Catalyst for the Degradation of Orange II in Water. *Water Res.* **2014**, *66*, 473–485. [CrossRef]

22. Huang, Y.-H.; Huang, Y.-F.; Huang, C.-I.; Chen, C.-Y. Efficient Decolorization of Azo Dye Reactive Black B Involving Aromatic Fragment Degradation in Buffered Co^{2+}/PMS Oxidative Processes with a Ppb Level Dosage of Co^{2+}-Catalyst. *J. Hazard. Mater.* **2009**, *170*, 1110–1118. [CrossRef] [PubMed]

23. Tan, C.; Gao, N.; Deng, Y.; An, N.; Deng, J. Heat-Activated Persulfate Oxidation of Diuron in Water. *Chem. Eng. J.* **2012**, *203*, 294–300. [CrossRef]

24. Ji, Y.; Dong, C.; Kong, D.; Lu, J.; Zhou, Q. Heat-Activated Persulfate Oxidation of Atrazine: Implications for Remediation of Groundwater Contaminated by Herbicides. *Chem. Eng. J.* **2015**, *263*, 45–54. [CrossRef]

25. Dulova, N.; Kattel, E.; Trapido, M. Degradation of Naproxen by Ferrous Ion-Activated Hydrogen Peroxide, Persulfate and Combined Hydrogen Peroxide/Persulfate Processes: The Effect of Citric Acid Addition. *Chem. Eng. J.* **2017**, *318*, 254–263. [CrossRef]

26. Duan, X.; Sun, H.; Wang, S. Metal-Free Carbocatalysis in Advanced Oxidation Reactions. *Acc. Chem. Res.* **2018**, *51*, 678–687. [CrossRef]

27. Miao, J.; Sunarso, J.; Su, C.; Zhou, W.; Wang, S.; Shao, Z. $SrCo_{1-x}Ti_xO_{3-\delta}$ Perovskites as Excellent Catalysts for Fast Degradation of Water Contaminants in Neutral and Alkaline Solutions. *Sci. Rep.* **2017**, *7*, 44215. [CrossRef]

28. Oh, W.-D.; Lua, S.-K.; Dong, Z.; Lim, T.-T. Performance of Magnetic Activated Carbon Composite as Peroxymonosulfate Activator and Regenerable Adsorbent via Sulfate Radical-Mediated Oxidation Processes. *J. Hazard. Mater.* **2015**, *284*, 1–9. [CrossRef]

29. Rodriguez, S.; Vasquez, L.; Costa, D.; Romero, A.; Santos, A. Oxidation of Orange G by Persulfate Activated by Fe(II), Fe(III) and Zero Valent Iron (ZVI). *Chemosphere* **2014**, *101*, 86–92. [CrossRef] [PubMed]

30. Ghanbari, F.; Moradi, M. Application of Peroxymonosulfate and Its Activation Methods for Degradation of Environmental Organic Pollutants: Review. *Chem. Eng. J.* **2017**, *310*, 41–62. [CrossRef]

31. Wang, J.; Wang, S. Activation of Persulfate (PS) and Peroxymonosulfate (PMS) and Application for the Degradation of Emerging Contaminants. *Chem. Eng. J.* **2018**, *334*, 1502–1517. [CrossRef]

32. Zhang, C.; Zhao, P.; Liu, S.; Yu, K. Three-Dimensionally Ordered Macroporous Perovskite Materials for Environmental Applications. *Chin. J. Catal.* **2019**, *40*, 1324–1338. [CrossRef]

33. Zhou, D.; Zhou, T.; Tian, Y.; Zhu, X.; Tu, Y. Perovskite-Based Solar Cells: Materials, Methods, and Future Perspectives. *J. Nanomater.* **2018**, *2018*, 8148072. [CrossRef]

34. Assirey, E.A.R. Perovskite Synthesis, Properties and Their Related Biochemical and Industrial Application. *Saudi Pharm. J.* **2019**, *27*, 817–829. [CrossRef] [PubMed]

35. Grimaud, A.; May, K.J.; Carlton, C.E.; Lee, Y.-L.; Risch, M.; Hong, W.T.; Zhou, J.; Shao-Horn, Y. Double Perovskites as a Family of Highly Active Catalysts for Oxygen Evolution in Alkaline Solution. *Nat. Commun.* **2013**, *4*, 2439. [CrossRef] [PubMed]

36. Jia, F.-F.; Zhong, H.; Zhang, W.-G.; Li, X.-R.; Wang, G.-Y.; Song, J.; Cheng, Z.-P.; Yin, J.Z.; Guo, L.-P. A Novel Nonenzymatic ECL Glucose Sensor Based on Perovskite $LaTiO_3$-Ag0.1 Nanomaterials. *Sens. Actuators B Chem.* **2015**, *212*, 174–182. [CrossRef]

37. Li, H.; Zhao, Y.; Wang, Y.; Li, Y. $Sr_2Fe_{2-x}Mo_xO_{6-\delta}$ Perovskite as an Anode in a Solid Oxide Fuel Cell: Effect of the Substitution Ratio. *Catal. Today* **2016**, *259*, 417–422. [CrossRef]

38. Tavakkoli, H.; Yazdanbakhsh, M. Fabrication of Two Perovskite-Type Oxide Nanoparticles as the New Adsorbents in Efficient Removal of a Pesticide from Aqueous Solutions: Kinetic, Thermodynamic, and Adsorption Studies. *Microporous Mesoporous Mater.* **2013**, *176*, 86–94. [CrossRef]

39. Wang, G.; Cheng, C.; Zhu, J.; Wang, L.; Gao, S.; Xia, X. Enhanced Degradation of Atrazine by Nanoscale LaFe$_{1-x}$Cu$_x$O$_{3-\delta}$ Perovskite Activated Peroxymonosulfate: Performance and Mechanism. *Sci. Total Environ.* **2019**, *673*, 565–575. [CrossRef]

40. Gao, P.; Tian, X.; Nie, Y.; Yang, C.; Zhou, Z.; Wang, Y. Promoted Peroxymonosulfate Activation into Singlet Oxygen over Perovskite for Ofloxacin Degradation by Controlling the Oxygen Defect Concentration. *Chem. Eng. J.* **2019**, *359*, 828–839. [CrossRef]

41. Miao, J.; Li, J.; Dai, J.; Guan, D.; Zhou, C.; Zhou, W.; Duan, X.; Wang, S.; Shao, Z. Postsynthesis Oxygen Nonstoichiometric Regulation: A New Strategy for Performance Enhancement of Perovskites in Advanced Oxidation. *Ind. Eng. Chem. Res.* **2020**, *59*, 99–109. [CrossRef]

42. Li, X.; Li, M.; Ma, X.; Miao, J.; Ran, R.; Zhou, W.; Wang, S.; Shao, Z. Nonstoichiometric Perovskite for Enhanced Catalytic Oxidation through Excess A-Site Cation. *Chem. Eng. Sci.* **2020**, *219*, 115596. [CrossRef]

43. Lin, K.-Y.; Chen, Y.-C.; Lin, Y.-F. LaMO$_3$ Perovskites (M=Co, Cu, Fe and Ni) as Heterogeneous Catalysts for Activating Peroxymonosulfate in Water. *Chem. Eng. Sci.* **2017**, *160*, 96–105. [CrossRef]

44. Chen, T.; Zhu, Z.; Wang, Z.; Zhang, H.; Qiu, Y.; Yin, D.; Zhao, G. 3D Hollow Sphere-like Cu-Incorporated LaAlO$_3$ Perovskites for Peroxymonosulfate Activation: Coaction of Electron Transfer and Oxygen Defect. *Chem. Eng. J.* **2020**, *385*, 123935. [CrossRef]

45. Anku, W.W.; Mamo, M.A.; Govender, P.P. Phenolic Compounds in Water: Sources, Reactivity, Toxicity and Treatment Methods. In *Phenolic Compounds—Natural Sources, Importance and Applications*; IntechOpen, Ltd.: London, UK, 2017. [CrossRef]

46. Rao, Y.F.; Zhang, Y.; Han, F.; Guo, H.; Huang, Y.; Li, R.; Qi, F.; Ma, J. Heterogeneous Activation of Peroxymonosulfate by LaFeO$_3$ for Diclofenac Degradation: DFT-Assisted Mechanistic Study and Degradation Pathways. *Chem. Eng. J.* **2018**, *352*, 601–611. [CrossRef]

47. Zhang, Y.; Xia, Y.; Li, Q.; Qi, F.; Xu, B.; Chen, Z. Synchronously Degradation Benzotriazole and Elimination Bromate by Perovskite Oxides Catalytic Ozonation: Performance and Reaction Mechanism. *Sep. Purif. Technol.* **2018**, *197*, 261–270. [CrossRef]

48. Wang, Y.; Wang, L.; Liu, R.; Li, X. Casein Templated Synthesis of Porous Perovskite and Its Application in Visible-Light Photocatalytic Degradation of Methylene Blue. *Mater. Sci. Semicond. Process.* **2019**, *103*, 104597. [CrossRef]

49. Ben Hammouda, S.; Zhao, F.; Safaei, Z.; Srivastava, V.; Lakshmi Ramasamy, D.; Iftekhar, S.; Kalliola, S.; Sillanpää, M. Degradation and Mineralization of Phenol in Aqueous Medium by Heterogeneous Monopersulfate Activation on Nanostructured Cobalt Based-Perovskite Catalysts ACoO$_3$ (A=La, Ba, Sr and Ce): Characterization, Kinetics and Mechanism Study. *Appl. Catal. B Environ.* **2017**, *215*, 60–73. [CrossRef]

50. Guo, H.; Zhou, X.; Zhang, Y.; Yao, Q.; Qian, Y.; Chu, H.; Chen, J. Carbamazepine Degradation by Heterogeneous Activation of Peroxymonosulfate with Lanthanum Cobaltite Perovskite: Performance, Mechanism and Toxicity. *J. Environ. Sci.* **2020**, *91*, 10–21. [CrossRef]

51. Thommes, M.; Kaneko, K.; Neimark, A.V.; Olivier, J.P.; Rodriguez-Reinoso, F.; Rouquerol, J.; Sing, K.S.W. Physisorption of Gases, with Special Reference to the Evaluation of Surface Area and Pore Size Distribution (IUPAC Technical Report). *Pure Appl. Chem.* **2015**, *87*, 1051–1069. [CrossRef]

52. Vijayaraghavan, T.; Bradha, M.; Babu, P.; Parida, K.M.; Ramadoss, G.; Vadivel, S.; Selvakumar, R.; Ashok, A. Influence of Secondary Oxide Phases in Enhancing the Photocatalytic Properties of Alkaline Earth Elements Doped LaFeO$_3$ Nanocomposites. *J. Phys. Chem. Solids* **2020**, *140*, 109377. [CrossRef]

53. Amiri, O.; Salar, K.; Othman, P.; Rasul, T.; Faiq, D.; Saadat, M. Purification of Wastewater by the Piezo-Catalyst Effect of PbTiO$_3$ Nanostructures under Ultrasonic Vibration. *J. Hazard. Mater.* **2020**, *394*, 122514. [CrossRef] [PubMed]

54. Afzal, S.; Quan, X.; Zhang, J. High Surface Area Mesoporous Nanocast LaMO$_3$ (M=Mn, Fe) Perovskites for Efficient Catalytic Ozonation and an Insight into Probable Catalytic Mechanism. *Appl. Catal. B Environ.* **2017**, *206*, 692–703. [CrossRef]

55. Chen, H.; Xu, Y.; Zhu, K.; Zhang, H. Understanding Oxygen-Deficient La$_2$CuO$_4$-Δperovskite Activated Peroxymonosulfate for Bisphenol A Degradation: The Role of Localized Electron within Oxygen Vacancy. *Appl. Catal. B Environ.* **2021**, *284*. [CrossRef]

56. Zhu, M.; Miao, J.; Guan, D.; Zhong, Y.; Ran, R.; Wang, S.; Zhou, W.; Shao, Z. Efficient Wastewater Remediation Enabled by Self-Assembled Perovskite Oxide Heterostructures with Multiple Reaction Pathways. *ACS Sustain. Chem. Eng.* **2020**, *8*, 6033–6042. [CrossRef]

57. Miao, J.; Sunarso, J.; Duan, X.; Zhou, W.; Wang, S.; Shao, Z. Nanostructured Co-Mn Containing Perovskites for Degradation of Pollutants: Insight into the Activity and Stability. *J. Hazard. Mater.* **2018**, *349*, 177–185. [CrossRef]

58. Miao, J.; Duan, X.; Li, J.; Dai, J.; Liu, B.; Wang, S.; Zhou, W.; Shao, Z. Boosting Performance of Lanthanide Magnetism Perovskite for Advanced Oxidation through Lattice Doping with Catalytically Inert Element. *Chem. Eng. J.* **2019**, *355*, 721–730. [CrossRef]

59. Lu, S.; Wang, G.; Chen, S.; Yu, H.; Ye, F.; Quan, X. Heterogeneous Activation of Peroxymonosulfate by LaCo$_{1-x}$Cu$_x$O$_3$ Perovskites for Degradation of Organic Pollutants. *J. Hazard. Mater.* **2018**, *353*, 401–409. [CrossRef]

60. Xu, Y.; Ai, J.; Zhang, H. The Mechanism of Degradation of Bisphenol A Using the Magnetically Separable CuFe$_2$O$_4$/Peroxymonosulfate Heterogeneous Oxidation Process. *J. Hazard. Mater.* **2016**, *309*, 87–96. [CrossRef]

61. Luo, X.; Bai, L.; Xing, J.; Zhu, X.; Xu, D.; Xie, B.; Gan, Z.; Li, G.; Liang, H. Ordered Mesoporous Cobalt Containing Perovskite as a High-Performance Heterogeneous Catalyst in Activation of Peroxymonosulfate. *ACS Appl. Mater. Interfaces* **2019**, *11*, 35720–35728. [CrossRef]

62. Sádaba, I.; López Granados, M.; Riisager, A.; Taarning, E. Deactivation of Solid Catalysts in Liquid Media: The Case of Leaching of Active Sites in Biomass Conversion Reactions. *Green Chem.* **2015**, *17*, 4133–4145. [CrossRef]

63. Okuhara, T. Water-Tolerant Solid Acid Catalysts. *Chem. Rev.* **2002**, *102*, 3641–3666. [CrossRef] [PubMed]

64. Sádaba, I.; Ojeda, M.; Mariscal, R.; Fierro, J.L.G.; Granados, M.L. Catalytic and Structural Properties of Co-Precipitated Mg-Zr Mixed Oxides for Furfural Valorization via Aqueous Aldol Condensation with Acetone. *Appl. Catal. B Environ.* **2011**, *101*, 638–648. [CrossRef]

65. Cicco, N.; Lattanzio, V. The Influence of Initial Carbonate Concentration on the Folin-Ciocalteu Micro-Method for the Determination of Phenolics with Low Concentration in the Presence of Methanol: A Comparative Study of Real-Time Monitored Reactions. *Am. J. Anal. Chem.* **2011**, *2*, 840–848. [CrossRef]